

## Full Length Article

## 3D-printed phononic crystal lens for elastic wave focusing and energy harvesting

S. Tol<sup>a</sup>, F.L. Degertekin<sup>b</sup>, A. Erturk<sup>b,\*</sup><sup>a</sup> Department of Mechanical Engineering, University of Michigan, Ann-Arbor, MI 48109-2125, United States<sup>b</sup> G. W. Woodruff School of Mechanical Engineering, Georgia Institute of Technology, Atlanta, GA 30332-0405, United States

## ARTICLE INFO

## Keywords:

Energy harvesting  
Phononics  
Metamaterials  
Wave propagation  
3D printing

## ABSTRACT

We explore elastic wave focusing and enhanced energy harvesting by means of a 3D-printed Gradient-Index Phononic Crystal Lens (GRIN-PCL) bonded on a metallic host structure. The lens layer is fabricated by 3D printing a rectangular array of cylindrical nylon stubs with varying heights. The stub heights are designed to obtain a hyperbolic secant distribution of the refractive index to achieve the required phase velocity variation in space, hence the gradient-index lens behavior. Finite element simulations are performed on composite unit cells with various stub heights to obtain the lowest antisymmetric mode Lamb wave band diagrams, yielding a correlation between the stub height and refractive index. The elastic wave focusing performance of lenses with different design parameters (gradient coefficient and aperture size) is simulated numerically under plane wave excitation. It is observed that the focal points of the wider aperture lens designs have better consistency with the analytical beam trajectory results. Experiments are conducted using a PA2200 nylon lens bonded to an aluminum plate to demonstrate wave focusing and enhanced energy harvesting within the 3D-printed GRIN-PCL domain. The piezoelectric energy harvester at the focal region of the GRIN-PCL produces 3 times more power output than the baseline harvester at the same distance in the flat plate region. The results show that 3D printing can provide a simple and practical method for implementing phononic crystal concepts with minimal modification of the host structure.

## 1. Introduction

Piezoelectric energy harvesting by converting ambient vibrations into low-power electricity has been explored by many researchers over the past two decades. The harvesting of standing waves in structures at a fixed position in space has been well studied via linear and nonlinear vibration energy harvesting methods [1–4]. Besides such standing waves, elastic energy in engineered structures is often manifested as a flowing energy in the form of propagating waves. Understanding the effective harvesting of such propagating waves and establishing efficient energy harvesting schemes for those scenarios requires a different approach to energy harvesting problem as compared to the conventional vibration-based energy harvesters in the form of linear or nonlinear cantilevers under persistent excitation. In a previous study of the authors [5], wave approach to energy harvesting was explored to extract the maximum electrical power in propagating wave scenarios including transient excitations. A fully coupled electroelastic modeling framework [5] was developed and experimentally validated to analyze the efficiency of elastic wave-to-electric energy conversion while

reducing the travelling waves reflected from and transmitted through the harvester domain.

Relatively few researchers have explored elastic/acoustic wave energy harvesting with a focus on phononic crystals [6–11], locally resonant metamaterials [12], quarter-wavelength resonators [13], and Helmholtz resonators [14–16]. In elastic wave energy harvesting, it is of interest to improve the efficiency by developing proper strategies for the localization and focusing of propagating waves. To this end, researchers have implemented parabolic and elliptical mirrors composed of acoustic scatterers [17–20] in order to reflect and focus propagating flexural waves (e.g.  $A_0$  mode Lamb wave) and thereby enhance the electrical response. Refraction characteristics can also be tailored to focus the wave energy via gradient-based concepts [21,22].

Lin et al. [23] proposed a Gradient-Index Phononic Crystal Lens (GRIN-PCL) by embedding solid cylinders with different elastic moduli in an epoxy medium, resulting in a hyperbolic secant distribution of the refractive index in the direction perpendicular to that of wave propagation, which bends the incident waves gradually toward the center axis. As a result, the wave energy converges at a focal spot along the

\* Corresponding author.

E-mail address: [alper.erturk@me.gatech.edu](mailto:alper.erturk@me.gatech.edu) (A. Erturk).

center where the refractive index is the highest (or the wave speed is the lowest). In another work, Wu et al. [24] numerically demonstrated the focusing of  $A_0$  mode Lamb waves in a perforated silicon GRIN-PCL plate, which was further explored numerically and experimentally by Zhao et al. [25]. Inspired by these efforts (i.e. to leverage them in energy harvesting), recently we presented GRIN-PCL design concepts and experiments for the enhancement of elastic wave energy focusing and harvesting in thin structures [21,22]. It was shown [21,22] that the harvested power can be increased by more than an order of magnitude using GRIN-PCL that employed blind holes as unit cells (as compared to the baseline case of energy harvesting on a flat plate without the lens).

In the existing literature, GRIN lenses for elastic wave focusing have been implemented by modification of the host structure via periodically arranged stubs of different heights or diameters, perforation via holes of varying size, and continuous thickness variation, among others [21–27]. Most of these concepts result in significant modification of the original host structure, which may not be desirable in many engineering applications (especially in light-weight structures). Recent advances in additive manufacturing has initiated a new era for the design, fabrication, and integration of metamaterials and phononic crystals via 3D-printed configurations. For instance, researchers have exploited additive manufacturing techniques to fabricate multi-material and complex-shaped metamaterials for vibration mitigation [28,29]. 3D-printing can also enable lightweight lens structures that can easily be integrated to a host structure [30].

In the following, we present a 3D-printed GRIN-PCL for elastic wave focusing and energy harvesting. The particular 3D-printed lens layer discussed here consists of an array of nylon stubs with varying heights along the direction perpendicular to that of wave propagation. Stub heights are designed to have a hyperbolic secant gradient distribution of the refractive index profile as obtained from finite element simulations of the lowest antisymmetric mode Lamb wave band diagram. Both numerical simulations and experimental results of the wave field are presented, and piezoelectric energy harvesting performance enhancement is demonstrated experimentally.

## 2. Unit cell design and phononic crystal lens

The design methodology of the GRIN phononic crystal lens (Fig. 1) originates from the optics counterpart of the problem. Here, we change the elastic properties of the composite plate by varying the height of 3D printed stubs in the unit cell in the lateral direction ( $y$ -direction) of the lens (perpendicular to the direction of wave propagation) which is then periodically repeated in the direction of wave propagation ( $x$ -direction). Stub heights are tailored according to a hyperbolic refractive index distribution which is defined as [23]

$$n(y) = n_0 \operatorname{sech}(\alpha y) \quad (1)$$

where  $n_0$  is the refractive index along the center axis and  $\alpha$  is the gradient coefficient. The refractive index can be calculated from the

ratio of the phase velocities in the homogenous aluminum plate and the composite unit cell at the design frequency (which can be obtained from dispersion curves of the  $A_0$  Lamb wave mode):

$$n = \frac{v}{v_{\Gamma X}} \quad (2)$$

where  $v_{\Gamma X}$  is the phase velocity along the  $\Gamma X$  direction ( $x$ -direction) in the composite PC and  $v$  is the reference phase velocity of the  $A_0$  mode Lamb wave in the aluminum substrate plate. In order to obtain the  $A_0$  mode band structure, we used finite element modeling (via COMSOL Multiphysics®). The unit cell simulations were performed by applying Floquet periodicity at the sides of the unit cell as boundary conditions. The bi-layer composite unit cell is composed of a host structure (aluminum plate) with a thickness of  $h = 1$  mm and a 3D-printed structure (PA 2200 with a density of  $930 \text{ kg/m}^3$  and elastic modulus of  $1700 \text{ GPa}$ ) with a base layer of  $h_n = 0.8$  mm and a stub diameter of  $d_s = 4.375$  mm (in  $5 \text{ mm} \times 5 \text{ mm}$  unit cell, i.e.  $a = 5$  mm) as illustrated in Fig. 1(a). Second-order tetrahedral mesh elements (with 10 nodes per element) were used in unit cell simulations. The band structure was calculated for various stub heights,  $h_s$ , as shown in Fig. 1(b) by parametric sweeping of the wave vector between  $0$  to  $\pi/a$  and computing eigenfrequencies at each wavenumber value. After obtaining the correlation between the stub heights and the refractive indices of the unit cells (Fig. 1(c)) we designed the 3D-printed GRIN-PCL based on the refractive index profile at  $40 \text{ kHz}$  as shown in Fig. 2(a). Note that, for the 3D printing material (PA2200) used in this study and for the geometric parameters used, the maximum stub height is limited at  $2 \text{ mm}$  because a bandgap starts to form around  $55 \text{ kHz}$ . On the other hand, the minimum stub height is limited to  $0.25 \text{ mm}$  due to the 3D printing resolution. We determined the number of unit cells in the propagation direction by locating the focal point of the lens at the center. The first focal point of the lens is calculated at  $17.6a$  (i.e.  $\text{FP} = 2\pi/\alpha$ ) where the gradient coefficient is determined as  $\alpha = 0.089$  from the hyperbolic secant profile of the refractive index (Fig. 2(a)). In the final design with 35 unit cells in the propagation direction and 11 unit cells in the lateral direction ( $175 \text{ mm} \times 55 \text{ mm}$  lens domain), the refractive index values were calculated as  $n = [1.115, 1.111, 1.098, 1.076, 1.048, 1.013]$  corresponding to stub heights  $h_s = [2, 1.96, 1.86, 1.66, 1.26, 0.25] \text{ mm}$ , at  $y = [0, \pm 1a, \pm 2a, \pm 3a, \pm 4a, \pm 5a]$ , respectively.

As a preliminary validation of the 3D-printed GRIN-PCL design (Fig. 2(b)), we used the analytical solution [31] to derive the beam trajectory within the lens domain. According to the solution for the ray trajectory in a planar waveguide, the beam profile can be calculated using:

$$y(x) = \frac{1}{\alpha} \sin^{-1}(u_0 H_f(x) + \dot{u}_0 H_a(x)) \quad (3)$$

$$H_f(x) = \cos(\alpha x) \quad (4)$$

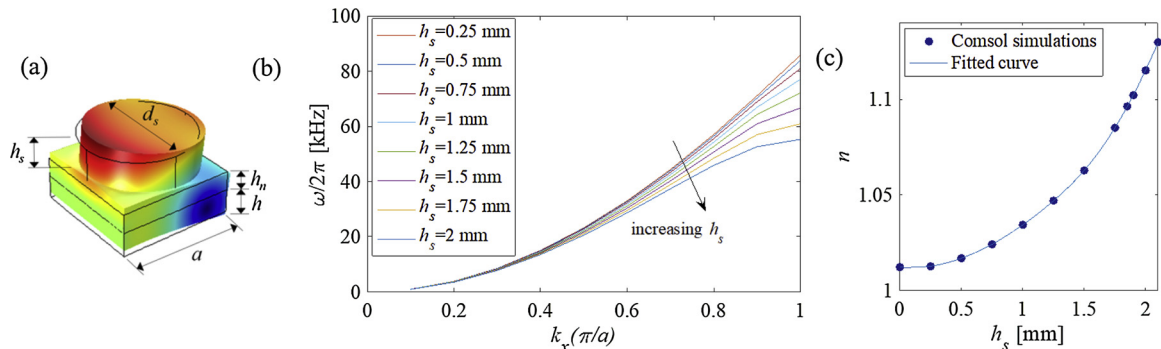


Fig. 1. (a) Composite unit cell; (b) band structure of  $A_0$  mode Lamb wave propagating along the  $\Gamma X$  orientation ( $x$ -direction); and (c) refractive index vs. stub height of the unit cells.

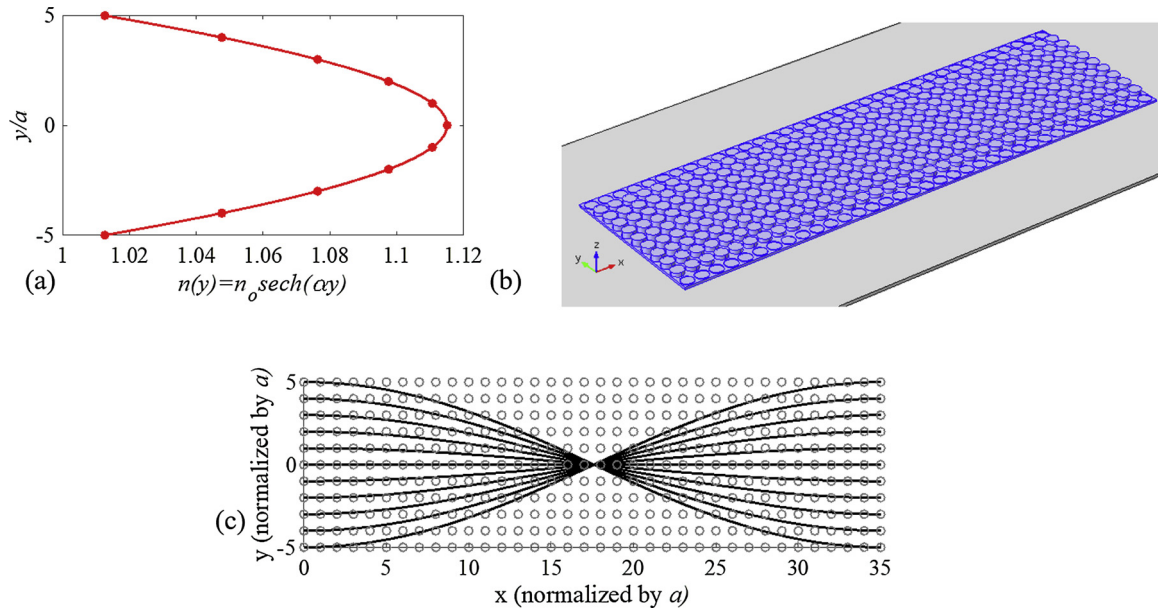


Fig. 2. (a) Hyperbolic secant distribution of the refractive index profile (dots represent the refractive index distribution used in the design); (b) 3D-printed GRIN-PCL designed with varying stub heights; and (c) analytical beam trajectory.

$$H_a(x) = \frac{\sin(\alpha x)}{\alpha} \quad (5)$$

where  $u_0$  is the ray position and  $\dot{u}_0$  is the slope of the ray at  $x = 0$ , and  $H_f(x)$  and  $H_a(x)$  are the positions of the field and axial rays, respectively. The ray trajectory analysis results in the first focal point at  $17.6a$  as shown in Fig. 2(c) which is consistent with the focal point obtained from the gradient coefficient.

### 3. Numerical simulations of wave field and focusing

Time-domain analysis was numerically performed in order to obtain the out-of-plane velocity field and verify wave focusing in the 3D-printed GRIN-PCL. A line source was modeled to excite the aluminum plate by acting as a boundary load with 7 cycles of sine burst with a Gaussian pulse envelope forcing at a center frequency of 40 kHz (the design frequency) with 20 kHz bandwidth; hence, the aforementioned bandgap frequencies are avoided (Fig. 1(b)). Low reflection boundary condition is applied at the end boundary. Second-order tetrahedral mesh elements (with 10 nodes per element) were used in the finite element simulations. Mesh size was set to satisfy 7 mesh elements per wavelength and a Courant-Friedrichs-Lewy number of 0.2 was selected to set the time step (so that the wave was equally resolved in space resulting in the optimal solution). Out-of-plane velocity wave fields were obtained from the time-domain analysis. Instantaneous velocity fields presented in Fig. 3 shows that as the plane wave incident upon the 3D-printed GRIN-PCL propagates in the lens, it travels faster at the edges and slower around the center. Plane wave energy converges toward the focal point where the refractive index is the highest or the wave speed is the lowest as it propagates in the lens domain (and then diverges after the focal point as expected from Fig. 2(c)). Also, an analysis of the reflected wavefronts assures that the incident wave field is focused to harvester spot without significant reflection from the lens domain (which is only ~10% in amplitude).

As illustrated in Fig. 4, comparison of the numerical RMS (root-mean-square) wave field and the analytical ray trajectories reveals that the focal point is obtained at  $20.6a$  which is larger than the beam trajectory results at  $17.6a$ . The difference might be due to the diffraction effects which are not modeled in analytical ray tracing. In addition, optimizing the unit cell size with a denser distribution in the refractive index profile may enhance the agreement between the ray trajectory

predictions and the finite element analysis (which is worth exploring but outside the scope of the current work). With the current lens design, the RMS intensity of the sum of the velocity field at the focal point (within a half-wavelength size circular region) is calculated to be 1.7 times larger than that of the flat plate counterpart at the same distance, confirming the improvement due to focusing. Next, we explore different lens designs in terms of controlling the focal distance and aperture size at the same design frequency and unit cell size (for the same material parameters) and examine their effect on the wave focusing performance of the 3D-printed GRIN-PCL.

In the first case study, we designed three different lenses with different gradient coefficients by changing the stub height distributions within the same aperture size (11 unit cell wide). The refractive index distributions and their corresponding stub height variations are illustrated in Fig. 5. For instance, for smaller gradient coefficients (larger focal depths), the heights of the center stubs are decreased to 1.52 mm and 1.1 mm while the heights of the edge stubs are kept the same at 0.25 mm.

According to the refractive index variations, the gradient coefficients are 0.089, 0.064, and 0.045 resulting in the focal depth predictions of  $17.6a$ ,  $24.6a$  and  $35.2a$ , respectively. In order to assess the wave focusing performance associated with these designs, time-domain simulations were performed. As illustrated in Fig. 6, we observe that the focusing neck and thickness increases as the focal depth increases. Also, as the focusing neck increases we see that the maximum wave intensity point in the focal region shifts away from the predicted values due to the dispersive nature of the flexural waves (17%, 20%, and 21% deviation from the beam trajectory prediction). Hence, if the focusing depth is critical in terms of wave focusing, then the GRIN-PCL with a larger gradient coefficient should be preferred. On the other hand, for all cases with the same lens aperture, similar wave focusing intensities are obtained in terms of the RMS wave field comparisons.

In the second case study, we designed two GRIN-PCLs with different aperture sizes (11 and 15 unit cells wide) while keeping the same gradient coefficient (hence the same focal depth). The refractive index distributions of the lenses are shown in Fig. 7. According to these refractive index variations, the gradient coefficient is 0.064 resulting in the focal depth prediction of  $24.6a$ . The 11 and 15 cells wide designs consist of stubs with height variations between 1.5-0.25 mm and 2-0.25 mm, respectively. Again, we performed numerical simulations to

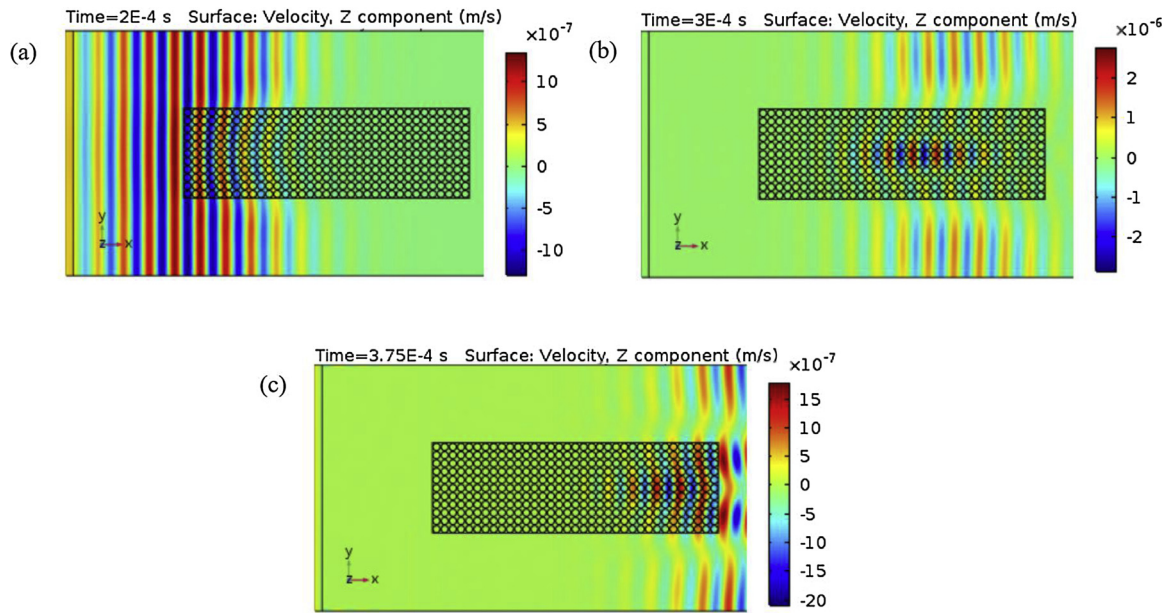


Fig. 3. Numerical simulation of the instantaneous wave fields at (a) 200  $\mu$ s; (b) 300  $\mu$ s; and (c) 375  $\mu$ s.

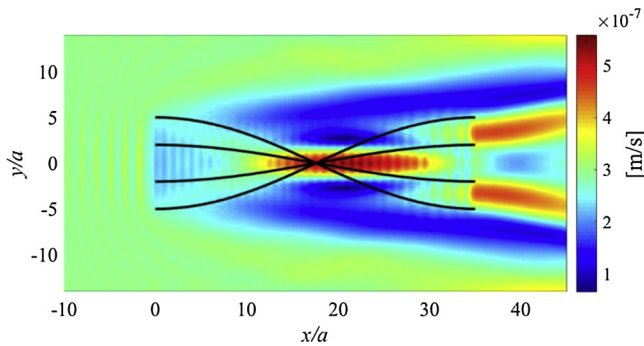


Fig. 4. RMS wave field from the numerical simulations.

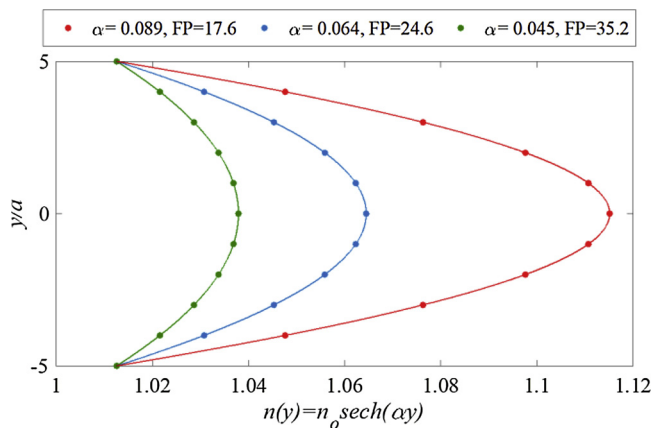


Fig. 5. Refractive index distributions for 11 unit cell wide lenses with different focal points (FPs) (markers represent the refractive index distribution used in the design).

assess the wave focusing performance. As observed in the RMS velocity wave fields of both lenses in Fig. 8, as the aperture size increases, the focusing intensity ratio increases from 1.7 to 1.9. Due to the larger aperture, the focus neck and thickness decrease which results in a better agreement in terms of predicting the focal depth with the analytical beam solution (deviation from the beam trajectory prediction decreases

from 20% to 12%). Hence, we can conclude that in order to have short focus necks and better wave focusing performance, wider lenses should be preferred. Furthermore, in order to design wide aperture lenses with shorter focal depths, the variation in the refractive index should be larger (however, for PA2200 material used in this study, the maximum stub height is limited to 2 mm due to bandgap formation close to the target frequency as previously mentioned). Hence, different materials can be used to create wide aperture lenses with shorter focal depths which agree well with the analytical ray trajectory results. Overall, numerical wave field simulations gives more accurate information on the focusing results.

#### 4. Experimental results and energy harvesting performance

To demonstrate experimental feasibility of 3D-printed GRIN-PCL, the particular compact design (175 mm  $\times$  55 mm, 11 unit cells wide lens with FP at 17.6a) described in Figs. 3–4 was fabricated using PA2200 (by EOS) via selective laser sintering. The bounding box of the 3D printer was 650 mm  $\times$  350 mm  $\times$  550 mm with an accuracy of  $\pm$  0.15 mm + 0.15% for the longest axis. Based on the resolution of the printer (0.1 mm), the minimum wall thickness was recommended as 0.7 mm, while the minimum embossed detail was recommended as 0.2 mm high and wide (which were taken into account during the design phase of the lens). The fabricated 3D printed lens layer is then bonded to the aluminum plate as shown in Fig. 9 with vacuum bonding procedure by applying a thin layer of epoxy between 3D printed layer and aluminum and allowing it to cure for 12 h under vacuum. 3M ScotchWeld™ DP460 two-part epoxy was chosen for bonding layer due to its high shear strength (27.58 MPa when bonded to aluminum). Similarly, a line array consisting of 18 piezoelectric transducers (5 mm  $\times$  0.4 mm from STEMiNC Corp.) was bonded to the aluminum plate by vacuum bonding which is used to generate the plane wave excitation.

Wave field experiments were performed with a Polytec PSV-400 scanning laser Doppler vibrometer (LDV) and the out-of-plane component of the velocity was measured over a grid of points covering the GRIN-PCL domain with a similar setup described in detail in previous work by the authors [21]. RMS wave field was obtained by integrating the measured velocity over time which is shown in Fig. 10 for a range of excitation frequencies (40–70 kHz). Wave focusing in the lens domain is clearly observed, with the best focusing performance obtained around

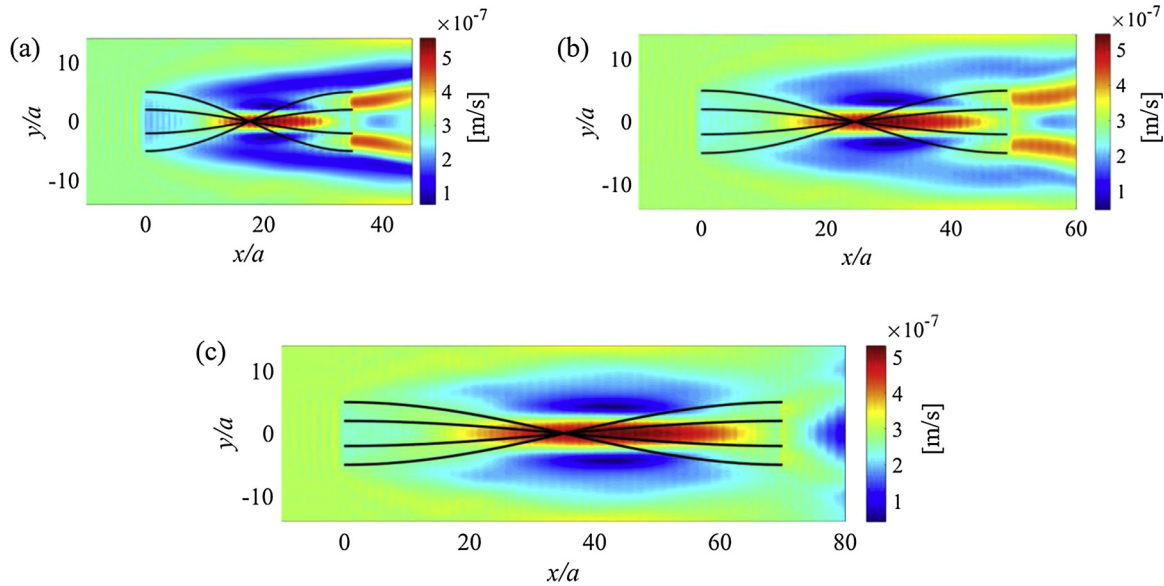


Fig. 6. RMS wave fields for the 11 unit cell wide lens designs with focal points at (a) 17.6a; (b) 24.6a; and (c) 35.2a (yielding the gradient coefficients of 0.089, 0.064, and 0.045, respectively).

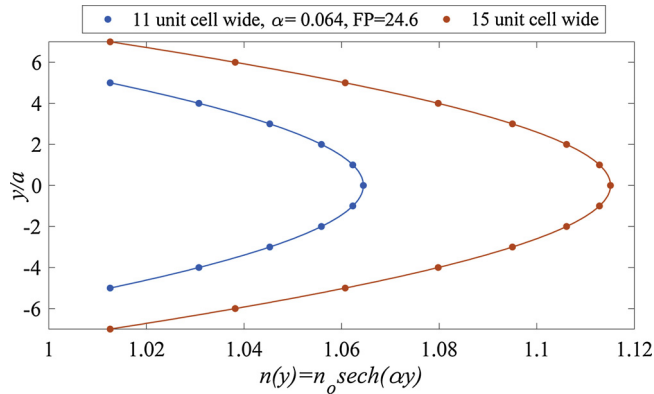


Fig. 7. Refractive index distributions for 11 and 15 unit cell wide lenses with the same focal points (markers represent the refractive index distribution used in the design).

55 kHz. The mismatch in terms of the frequency (relative to the numerical results) can be attributed to the imperfections in the experimental setup shown in Fig. 9, which includes non-ideal lens geometry due to the limitations of the 3D printing fabrication process (resolution, minimum layer thickness, etc.) and the nylon material resulting in a thicker base layer, leading to higher reflection and imperfections in the geometry of the stubs as well as non-planar incident wave field. Combined with the effect of thin epoxy bonding layer, the effect of this relatively thick (0.8 mm) base layer and stubs on the refractive index distribution are more pronounced for the thin (1 mm) aluminum host structure. Overall, these factors result in a different refractive index

distribution as compared to the original design. Nevertheless, the experimental wave field at 55 kHz agrees well with the predictions in terms of the focusing neck and intensity.

In order to assess the enhancement in energy harvesting performance through wave focusing in the 3D-printed GRIN-PCL, identical half-wavelength piezoelectric energy harvester disks (7 mm × 0.4 mm from STEMiNC Corp.) were vacuum-bonded at the focal region of the lens and in the flat plate region (i.e. baseline setting) at the same distance from the excitation source as shown in Fig. 11. Energy harvesting experiments were performed with resistor sweep tests under the plane wave excitation with 7 cycles of sine burst at 55 kHz. In the experiments, the bottom and top electrodes of the piezoelectric harvesters were shunted to a range of resistive electrical loads (2 kΩ - 7 kΩ) covering the optimal conditions of both the GRIN-PCL-enhanced harvester and the baseline harvester. The voltage across the resistors was measured simultaneously with an oscilloscope (Tektronix TDS5034) and the average power outputs of the harvesters were calculated.

Fig. 12(a) shows the measured voltage output time series for the baseline and GRIN-PCL harvesters under optimal resistive loads of 4.8 kΩ and 4.6 kΩ, respectively. As a result of elastic wave focusing in the 3D-printed GRIN-PCL, the harvested power is increased by 2.84 times as shown in Fig. 12(b) as compared to the baseline setting on the flat plate. This is in agreement with the estimated ~1.7 fold increase in the velocity field amplitude measured at the focal point of the lens (since power is proportional to the square of the amplitude). Hence, structure-borne wave energy harvesting can be enhanced significantly by integrating piezoelectric energy harvesters within the 3D-printed GRIN-PCL.

It is worth mentioning that laboratory scale experiments were performed at 55 kHz range which is a relatively high frequency as

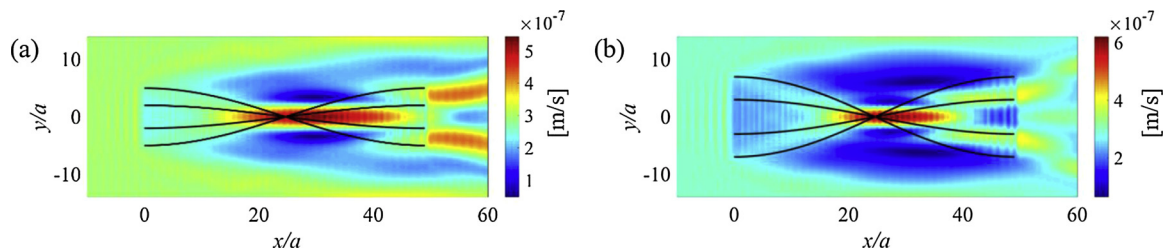


Fig. 8. RMS wave fields for the GRIN-PCL lens of different widths: (a) 11 unit cell wide and (b) 15 unit cell wide.

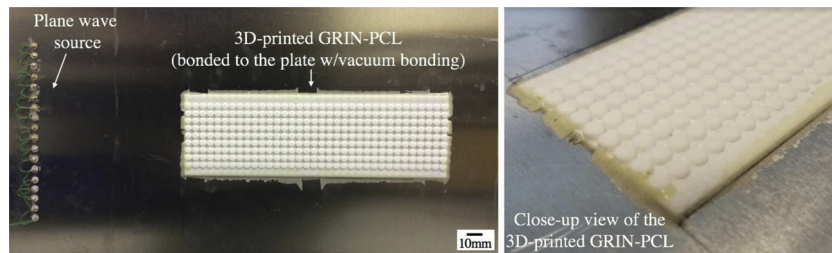


Fig. 9. 3D-printed GRIN-PCL structure and a close-up view (the velocity field is measured on the other face of the plate that is covered with retroreflective tape).

compared to the ambient vibration spectrum for energy harvesting. The design frequency of such crystal-based lens design can be reduced by increasing the size of the unit cells (due to the wavelength dependency of the phononic crystals), which would result in very high dimensions at ambient vibration frequencies (~hundreds of Hz). Alternatively, locally resonant (LR) unit cells [32–34] can be exploited to enable low-frequency elastic wave focusing via LR lens concepts [35] which is a topic for a future study. Beyond energy harvesting, 3D-printed lens designs proposed in this study can be useful in sensing and structural health monitoring applications, among others.

5. Conclusions

In this study, we explored a 3D-printed GRIN-PCL (Gradient-Index Phononic Crystal Lens) as an alternative to conventional GRIN-PCL

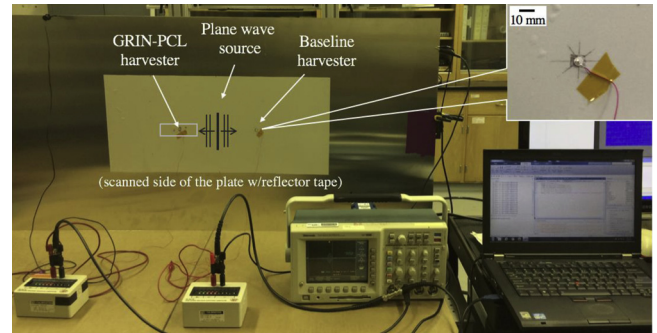


Fig. 11. Experimental setup and close-up view of the piezoelectric harvester along with a view of the scanned area.

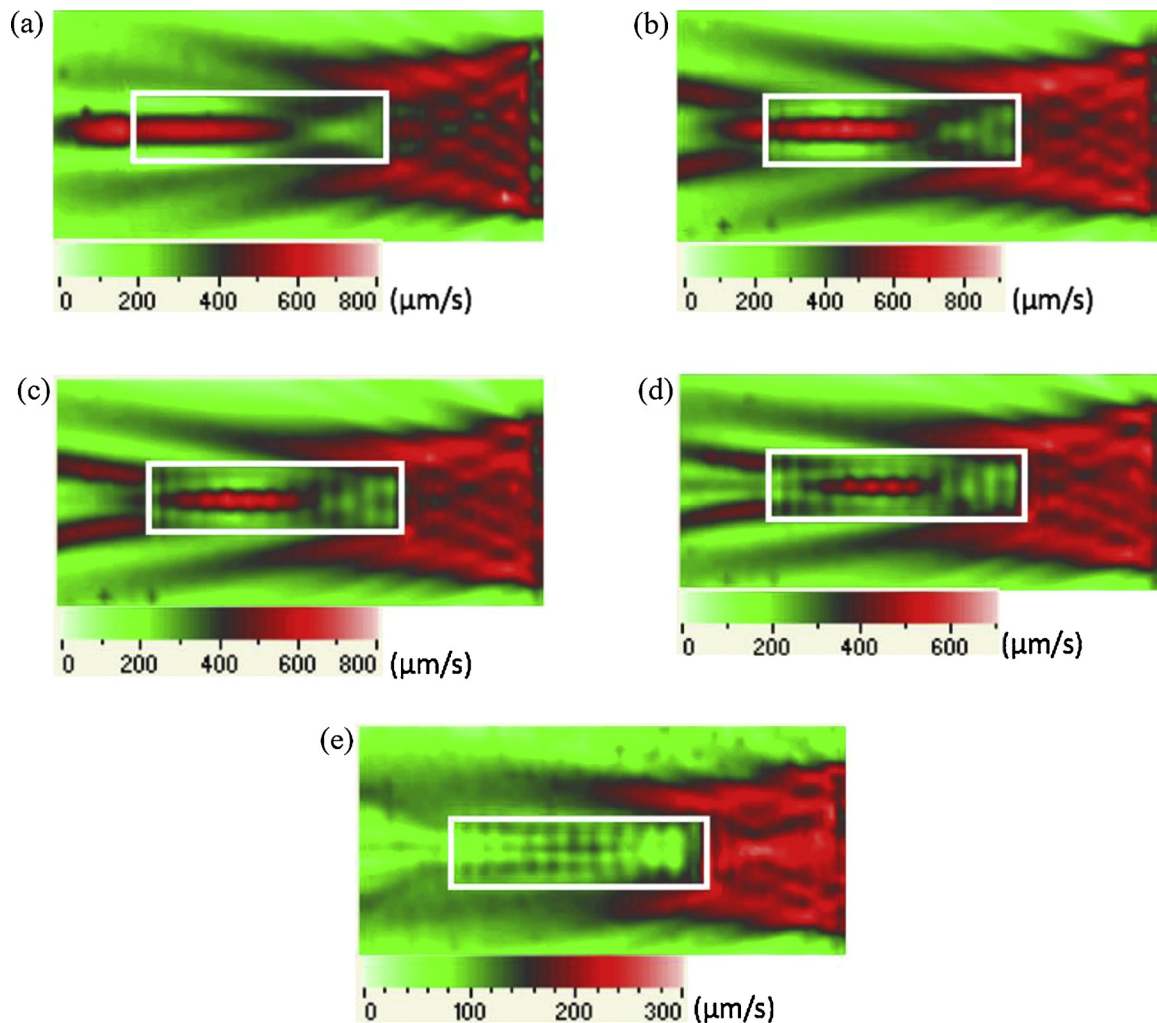


Fig. 10. Experimental RMS wave fields at (a) 40 kHz; (b) 50 kHz; (c) 55 kHz; (d) 60 kHz; and (e) 70 kHz.

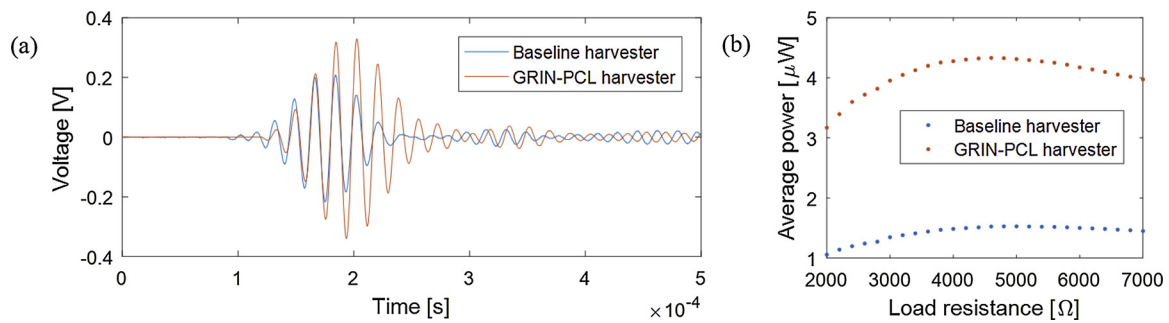


Fig. 12. Energy harvesting performance comparison: (a) Voltage output under optimal resistive loading and (b) average power output vs. load resistance.

designs and demonstrated its use in energy harvesting. The proposed lens region is composed of bi-layer composite unit cells including a 3D printed layer (PA2200) bonded to the aluminum structure to achieve a hyperbolic secant profile distribution of the refractive index. We investigated limitations of this approach in different lens designs for the given material combination. Wider aperture lens focuses more energy, as expected, and gives better agreement between the beam trajectory method and the numerical finite element simulations in predicting the focal distance. On the other hand, as the gradient coefficient increases within the same aperture size lenses, the focusing neck becomes narrower, resulting in better predictions from the beam trajectory solution. The 3D-printed lens layer successfully focuses  $A_0$  mode Lamb waves and achieves significantly enhanced energy harvesting. We designed, fabricated, and experimentally demonstrated a 3D-printed GRIN-PCL-based harvester. The harvested power output is enhanced nearly 3 times as compared to the baseline harvester in the flat plate domain. Energy harvesting can be further enhanced by optimizing the 3D-printed lens design in terms of using different 3D printing materials, unit cell dimensions, and aperture sizes for better focusing performance. In addition to avoiding major structural changes in the host structure for GRIN-PCL implementation (e.g. by perforation or substantial mass addition), 3D printing can offer simple but enhanced functionality by enabling embedded harvester/sensor designs.

## Acknowledgment

This work was supported in part by the National Science Foundation under Grant No. CMMI-1333978.

## References

- [1] S. Roundy, P.K. Wright, J.M. Rabaey, *Energy Scavenging for Wireless Sensor Networks With Special Focus on Vibrations*, Springer, New York, 2004.
- [2] S. Priya, D.J. Inman, *Energy Harvesting Technologies*, Springer, New York, 2009.
- [3] A. Erturk, D.J. Inman, *Piezoelectric Energy Harvesting*, Wiley, 2011.
- [4] N. Elvin, A. Erturk, *Advances in Energy Harvesting Methods*, Springer, 2013.
- [5] S. Tol, F.L. Degertekin, A. Erturk, Piezoelectric power extraction from bending waves: electroelastic modeling, experimental validation, and performance enhancement, *Wave Motion* 60 (2016) 20–34.
- [6] H. Lv, et al., Vibration energy harvesting using a phononic crystal with point defect states, *Appl. Phys. Lett.* 102 (2013) 034103.
- [7] W.C. Wang, et al., Acoustic energy harvesting by piezoelectric curved beams in the cavity of a sonic crystal, *Smart Mater. Struct.* 19 (2010).
- [8] L.Y. Wu, L.W. Chen, C.M. Liu, Acoustic energy harvesting using resonant cavity of a sonic crystal, *Appl. Phys. Lett.* 95 (2009).
- [9] S. Gonella, A.C. To, W.K. Liu, Interplay between phononic bandgaps and piezoelectric microstructures for energy harvesting, *J. Mech. Phys. Solids* 57 (3) (2009) 621–633.
- [10] Z.S. Chen, et al., Broadband characteristics of vibration energy harvesting using one dimensional phononic piezoelectric cantilever beams, *Phys. B: Condens. Matter* 410 (2013) 5–12.
- [11] C.J. Rupp, M.L. Dunn, K. Maute, Switchable phononic wave filtering, guiding, harvesting, and actuating in polarization-patterned piezoelectric solids, *Appl. Phys. Lett.* 96 (2010).
- [12] K. Mikoshiba, J.M. Manimala, C. Sun, Energy harvesting using an array of multifunctional resonators, *J. Intell. Mater. Syst. Struct.* 24 (2) (2012) 168–179.
- [13] B. Li, et al., Harvesting low-frequency acoustic energy using multiple PVDF beam arrays in quarter-wavelength acoustic resonator, *Appl. Acoust.* 74 (2013) 1271–1278.
- [14] S.B. Horowitz, et al., A MEMS acoustic energy harvester, *J. Micromech. Microeng.* 16 (S174) (2006).
- [15] F. Liu, et al., Acoustic energy harvesting using an electromechanical Helmholtz resonator, *J. Acoust. Soc. Am.* (2008).
- [16] A. Yang, et al., Enhanced acoustic energy harvesting using coupled resonance structure of sonic crystal and Helmholtz resonator, *Appl. Phys. Lett.* 12 (6) (2013).
- [17] M. Carrara, et al., Dramatic enhancement of structure-borne wave energy harvesting using an elliptical acoustic mirror, *Appl. Phys. Lett.* 100 (20) (2012) 204105.
- [18] M. Carrara, et al., Metamaterial-inspired structures and concepts for elastoacoustic wave energy harvesting, *Smart Mater. Struct.* 22 (6) (2013).
- [19] M. Carrara, et al., Fourier transform-based design of a patterned piezoelectric energy harvester integrated with an elastoacoustic mirror, *Appl. Phys. Lett.* 106 (2015) 013907.
- [20] S. Tol, F.L. Degertekin, A. Erturk, *Embedded Elastic Wave Mirrors for Enhanced Energy Harvesting*, IEEE Sensors, Orlando, FL, 2016.
- [21] S. Tol, F. Degertekin, A. Erturk, Gradient-index phononic crystal lens-based enhancement of elastic wave energy harvesting, *Appl. Phys. Lett.* 109 (6) (2016) 063902.
- [22] S. Tol, F. Degertekin, A. Erturk, Phononic crystal Luneburg lens for omnidirectional elastic wave focusing and energy harvesting, *Appl. Phys. Lett.* 111 (1) (2017) 013503.
- [23] S.-C.S. Lin, et al., Gradient-index phononic crystals, *Phys. Rev. B* 79 (9) (2009) 094302.
- [24] T.-T. Wu, et al., Focusing of the lowest antisymmetric Lamb wave in a gradient-index phononic crystal plate, *Appl. Phys. Lett.* 98 (17) (2011) 171911.
- [25] J. Zhao, et al., Efficient focalization of antisymmetric Lamb waves in gradient-index phononic crystal plates, *Appl. Phys. Lett.* 101 (26) (2012) 261905.
- [26] Y. Jin, et al., Simultaneous control of the  $S_0$  and  $A_0$  Lamb modes by graded phononic crystal plates, *J. Appl. Phys.* 117 (24) (2015) 244904.
- [27] Y. Jin, B. Djafari-Rouhani, D. Torrent, Gradient index phononic crystals and metamaterials, *Nanophotonics* (2019).
- [28] Y. Chen, et al., Broadband and multiband vibration mitigation in lattice metamaterials with sinusoidally-shaped ligaments, *Extreme Mech. Lett.* 17 (2017) 24–32.
- [29] K.H. Matlack, et al., Composite 3D-printed metastructures for low-frequency and broadband vibration absorption, *Proc. Natl. Acad. Sci.* 113 (30) (2016) 8386–8390.
- [30] S. Tol, F.L. Degertekin, A. Erturk, 3D-printed Lens for Structure-borne Wave Focusing and Energy Harvesting. In *SPIE Smart Structures and Materials + Nondestructive Evaluation and Health Monitoring*, International Society for Optics and Photonics, 2017.
- [31] C. Gómez-Reino, M.V. Perez, C. Bao, *Gradient-index Optics: Fundamentals and Applications*, Springer, Berlin, 2002.
- [32] Z. Liu, et al., Locally resonant sonic materials, *Science* 289 (5485) (2000) 1734–1736.
- [33] C. Sugino, et al., On the mechanism of bandgap formation in locally resonant finite elastic metamaterials, *J. Appl. Phys.* 120 (13) (2016) 134501.
- [34] C. Sugino, et al., A general theory for bandgap estimation in locally resonant metastructures, *J. Sound Vib.* 406 (2017) 104–123.
- [35] S. Tol, F.L. Degertekin, A. Erturk, Low-frequency elastic wave focusing and harvesting via locally resonant metamaterials, *ASME 2017 Conference on Smart Materials, Adaptive Structures and Intelligent Systems* (2017).